Section A-Research paper
ISSN 2063-5346

Dielectric and Magnetic Studies of Cerium Substituted Nanocrystaline Cu-Mg-Cr Spinel Ferrites

Mahesh Mahadev Gurav[a], Radhakrishanan Macchindranath Tigote[b], Appasaheb Wamanrao Suryawanshi[a]*

[a]Department of Chemistry, Shri Madhavarao Patil Mahavidyalaya, Murum 413605 Osmanabad, (Maharashtra) India. Email- maheshgrv0@gmail.com

[b]Department of Chemistry, Dr. Babasaheb Ambedkar Marathwada University, Sub campus, Osmanabad 413501, (Maharashtra) India. Email-rmtigote@gmail.com

[a*]Department of Chemistry, Shri Madhavarao Patil Mahavidyalaya, Murum 413605 Osmanabad, (Maharashtra) India. Email- sury44444@yahoo.com, Mob. No. +91-9860622353 (Corresponding Author)

Abstract

At room temperature, different compositions of nanocrystalline $Cu_{0.5}Mg_{0.5}Cr_{0.5}Ce_xFe_{1.5-x}O_4$ (x = 0.0, 0.05, 0.10, 0.15) were prepared using the sol-gel method. Cubic spinel nanoparticles were confirmed through X-ray diffraction (XRD) measurements. The secondary phase of CeO_2 was observed to increase in cerium content, as well as an increase in the lattice constant (7.831 Å to 7.881 Å) and a decrease in the crystalline size (28 nm to 26 nm) of the ferrites. TGA study revealed that the sample had a weight loss of up to 12.0 % and a thermal stability of 88.0 %. FTIR spectra showed the characteristic broad band between 500 and 1000 cm^{-1} for M-O bonding present in the ferrite sample. FE-SEM images revealed a spherical particle. HR- TEM also revealed the spherical shape with grain sizes ranging from 48 to 55 nm. The sample exhibited super paramagnetic behaviour as the saturation magnetization value increased due to an increase in the x-value of ferrite. Similarly, with an increase in frequency, the loss in dielectric properties of the samples was observed due to the change in the electrical conduction in the ferrites.

Keywords-Nanomaterials, spinel ferrite, magnetic properties, dielectric properties, Morphology

Introduction

Nano-scale ferrite particles have received a lot of attention because of their unique

structural, electrical, and chemical properties, as well as their applications in a variety of fields. Surface chemistry is another important aspect affecting the properties of nanoscale particles. Nanoscale ferrite particles have a high surface-to-volume ratio. Nanoscale ferrite particles have good electrical properties due to their high resistivity and minimal energy losses. Because each particle is considered a single domain below a critical size, the electrical properties are affected by particle size. Metal oxide nanoparticles have unusual optical, catalytic, and magnetic properties. Since spinel ferrites have ferromagnetic and semiconducting properties, they are classified as magnetic semiconductors. The chemical composition of ferrite nanoparticles affects their intrinsic magnetic properties, while their microstructure, which depends on the processing method of the ferrite, affects their extrinsic magnetic properties. Consequently, the chemical composition and processing method are critical factors in improving the physical properties of ferrites. Due to their narrow band gap and high surface area, nanoparticles are useful as photo catalysts. [1-11]

Spinel ferrites have the general formula AB_2O_4. In spinel ferrites, there are 32 octahedral sites, each surrounded by 6 oxygen ions, and 64 tetrahedral sites, each surrounded by 4 oxygen ions. They have both octahedral B and tetrahedral A sites. Their magnetic behaviour depends on the A and B sites of the cation. [12-17] A number of methods are used for the synthesis of ferrite nanoparticles. These methods include sol-gel, micro emulsion, chemical co-precipitation, the self-combustion method, the hydrothermal method, the ball milling method, the inverse micro emulsion method, the solid state reaction method, and the double sintering method.[18-22] The sol-gel method is the most widely used method because it is easy to use, provides good shape and controlled particle size, and controls the homogeneity of the compositions. Other advantages of this technology over others are its simplicity, cost efficiency, and low energy consumption.[23] Due to all these advantages of the sol-gel method over other methods, we use the sol-gel method for the synthesis of our spinel ferrite nanoparticles in the present work. Ferrites have drawn a lot of attention to heterogeneous advanced oxidation processes due to their good catalytic activity, thermal stability, surface oxygen mobility, low cost, natural abundance, and inexpensive separation from reaction mixtures.[24] Ferrites are applicable for microelectronics, humidity sensors, microwave reflections, high data storage materials, converters, switching appliances, and antenna frames due to their unique set of properties.[25, 26] Higher electrical resistivity, low power losses, and high magnetic responses made them suitable for high-frequency operational bands, power electronics, telecommunications, and inductor and transformer cores.[27] Aside from that,

spinel ferrite has clinical applications in hyperthermia, disease diagnosis, drug delivery systems, malignant tumours, magnetic resonance imaging, and iron deficiency treatment.[28, 29] The substitution of rare earth elements in spinel ferrite produces lattice distortion, which results in lattice strain. The spin coupling of 3D electrons and Fe^{3+}-Fe^{3+} interactions are responsible for the magnetic, optical, spectroscopic and electrical properties of rare earth doped spinel ferrites. However, rare earth metal (Re^{3+}-Fe^{3+}) interactions occur in spinel ferrites, which help to tune the magnetic properties and are useful in microwave devices, power transformers, gas sensing materials, and magnetic Photocatalytic and biological activities are also demonstrated by rare-earth-doped ferrite. As a result, many researchers have been drawn to the outstanding magnetic, optical, and electrical properties of RE-doped spinel ferrites. Rare earth lanthanides have high resistance and are thus excellent electrical insulators. They are commonly used to modify the structural, magnetic, and electrical properties of ferrites. Their substitute produced high DC resistivity, low electrical permittivity, and low dielectric loss.[30-37]

Thus, the present work focuses on the synthesis of cerium-doped spinel ferrites by the sol-gel method. The aim of the synthesis of cerium-doped spinel ferrite is to investigate the effects of doping with the rare earth element cerium ion and its distribution in the A and B sub lattices on the structural, magnetic, and morphological properties of the ferrite nanoparticles. The structural, magnetic, electrical, and morphological properties of sol-gel synthesised ferrite nanoparticles were investigated by TGA analysis, FT-IR study, X-ray diffraction, vibrating sample magnetometer, field emission scanning electron microscopy, transmission electron microscopy, and dielectric permittivity study.

Experimental

Materials

High-purity chemicals were bought from Himedia and used without additional purification. For each experiment, distilled water was used. A.R.-grade chemicals such as copper nitrate $Cu(NO_3)_2.6H_2O$, magnesium nitrate $Mg(NO_3)_3.6H_2O$, chromium nitrate $Cr(NO_3)_3.9H_2O$, iron nitrate $Fe(NO_3)_3.9H_2O$, and cerium nitrate $Ce(NO_3)_3.6H_2O$ are all precursors.

Synthesis of $Cu_{0.5}Mg_{0.5}Cr_{0.5}Fe_{1.5-x}O_4Ce_x$ nanoparticles

The sol-gel auto-combustion method was used to synthesize Cerium doped $Cu_{0.5}Mg_{0.5}Cr_{0.5}Fe_{1.5-x}O_4$ nanomaterials. Initially, copper nitride, magnesium nitride, chromium nitride, ferric nitride, and cerium nitride were taken and mixed with distilled water

in their weight proportions. During this process, citric acid was added as a chelating agent in the stoichiometric ratio of 1:3 while the solution was continuously stirred. The pH of the solution remained neutral after adding ammonia drop by drop. The mixture was next heated to 90 °C on a hot plate with magnetic stirring. After 6 hours, the solution becomes vigorous and converts to sol; after 1 hour, the solution transfers to gel. At this constant temperature, gel dries into powder. The resulting material was calcined for 6 hours at 800 °C.

Result and Discussion

Characterization

Thermo gravimetric analysis (TGA)

The weight change that occurs as a sample is heated at a constant rate is detected by thermo gravimetric analysis, which also detects thermal stability and the fraction of unstable components. Two main weight loss steps at 229 °C and 763 °C can be seen in the temperature range from room temperature. At 229 °C, an initial weight loss of ~3 % was observed for $Cu_{0.5}Mg_{0.5}Cr_{0.5}Fe_{1.5}O_4$ ferrite. This loss results from the elimination of physioadsobed and interlayer water as well as impurities from ferrite. Final degradation was observed at 763 °C with a weight loss of ~7 %. This loss is due to the formation of metal oxides. Thus, from the thermo gravimetric analysis, it is observed that synthesized $Cu_{0.5}Mg_{0.5}Cr_{0.5}Fe_{1.5}O_4$ ferrite is thermally stable without impurities. The synthesized material shows 88 % thermal stability, as shown in **Figure 1**.

Fourier Transform Infra – Red Spectroscopy (FT – IR)

The FT-IR spectra for all cubic spinel ferrite samples are shown in **Figure 2**. All sample spectra were observed in the 400-4000 cm^{-1} range. The formation of Ce doped Cu-Mg-Cr nanocrystalline ferrite was verified by the presence of two adsorption bands between 400 and 600 cm^{-1}. The higher adsorption band produced by M-O tetrahedral stretching vibrations is among these lower adsorption bands formed by octahedral M-O stretching vibrations. Tetrahedral M-O stretching vibration is in the range of 525-580 cm^{-1}, while the octahedral M-O stretching vibration is in the range of 441-475 cm^{-1}. The band at 1150 cm^{-1} is formed during the synthesis of a cerium-merged Fe-O bond.

X – Ray Diffraction Study (XRD)

Figure 3 shows the XRD pattern of $Cu_{0.5}Mg_{0.5}Cr_{0.5}Ce_xFe_{1.5-x}O_4$ ferrite nanoparticles. The x-ray diffraction pattern shows the diffraction peaks at (111), (220), (311), (222), (400), (422), (511), (440), (620), (533), and (444) for all concentration samples. The most intense peak was observed at (311) for all these samples. A similar XRD pattern has been observed

in the literature.[19] Some feeble CeO_2 peak reflections were also visible in the XRD pattern. As the intensity of the Ce doping increased, the size of the nanocrystals gradually decreased. The confirmation of the formation, which revealed that CeO_2 Peaks moved to the right side as the value increased, served as evidence for this. In the crystal lattice, Ce atoms primarily replaced Fe atoms at lower dopant values. The rise at x = 0.05 is thus barely perceptible. CeO_2, on the other hand, has a peak intensity that is more noticeable at higher amounts. Extra phases are precipitated and separated once elements of rare earths are introduced into the spinel lattice. Crystalline size (D) is calculated using the Sherer equation from the line broadening of the most intense peak (311).

$$D = \frac{0.9\lambda}{\beta COS\theta} \quad (1)$$

Where λ is the wavelength of the incident x-ray, D is particle size, θ is the diffraction angle, and β is the full width of the half maximum. From the analysis, it was clear that particle size decreases in the range from 28 nm to 26 nm with an increase in the doping concentration of Ce^{+3} in the ferrite. The lattice parameter was calculated by using the equation as follows:

$$a = dhkl\sqrt{h^2 + k^2 + l^2} \quad (2)$$

Where d_{hkl} is the interplanar distance for the obtained hkl values, Bragg's law equation was used to calculate interplanar distances

$$n\lambda = 2dSin\theta \quad (3)$$

The effect of an increase in the doping concentration of Ce^{+3} on lattice parameter values is shown in Figure. As the doping concentration of Ce^{+3} increases, the lattice parameter value increases from 7.831 Å to 7.881 Å. This is due to the doping of larger ionic radius Ce^{+3} (1.14 Å) at the site of lower ionic radius Fe^{+3} (0.63 Å) in spinal ferrite, which would cause an increase in the lattice parameter. With the use of the following relation, X-ray density and hopping length at tetrahedral and octahedral sites were calculated.

$$dx = \frac{8M}{a^3 N_A} \quad (4)$$

$$L_A = \frac{a\sqrt{3}}{4} \quad , \quad \text{and} \quad L_B = \frac{a\sqrt{2}}{3} \quad (5)$$

Where N_A is the Avogadro's constant, a is the lattice parameter, and M is the molar weight of the sample. The Hoping length of Tetrahedral and Octahedral sites increased as the concentration of Ce^{+3} ion increased. The x-ray density increases as the Ce^{+3} doping concentration increases. This resulted from the incorporation of the Ce^{+3} ion into ferrite, which increased the mass thickness and produced ferrite grains with a more subdued appearance. These grains were in line with improvements in the relative densities and

shrinkage width rates. Another explanation for the rise in x-ray density is the existence of phase CeO_2. The values of interplanar spacing, crystalline size, and hoping length of the octahedral and tetrahedral sites are listed in **Table 1**. The values of the lattice parameter, x-ray density, and unit cell volume are listed in **Table 2.**

Table 1. Variation of interplanar spacing, crystalline size and hoping length of $Cu_{0.5}Mg_{0.5}Cr_{0.5}Ce_xFe_{1.5-x}O_4$ nanoparticles

Sr. No.	Concentration (x)	Interplanar Spacing (Å)	Crystalline Size (nm)	Hoping length L_A	Hoping length L_B
1.	0.0	2.0653	28.19	3.391	5.538
2.	0.05	2.0669	27.43	3.404	5.559
3.	0.10	2.0782	27.38	3.411	5.571
4.	0.15	2.0790	26.16	3.412	5.573

Table 2. Lattice parameter, X-ray density and Unit cell volume of $Cu_{0.5}Mg_{0.5}Cr_{0.5}Ce_xFe_{1.5-x}O_4$ nanoparticles

Sr. No.	Concentration (x)	Lattice Parameter (Å)	X- ray density (gm cm^{-3})	Unit cell volume (cm^3)
1.	0.0	7.831	6.0210	480.3062
2.	0.05	7.862	6.0675	485.8472
3.	0.10	7.878	6.1426	489.0059
4.	0.15	7.881	6.2511	489.4902

Magnetic Study

Figure 5 shows the variation of magnetization against the applied external magnetic field. All observations were made while using a 15 Oe magnetic field at room temperature. **Table 3** shows the values of saturation magnetization, remanence magnetization, coercivity, squareness ratio, and anisotropy constant. The saturation magnetization and remanence magnetization values increase as the doping concentration of Ce^{+3} ions increase. The coercivity value decreases with increases in saturation magnetization. This correlation is given by the Brown equation as,

$$H_c = \frac{2k_1}{\mu_0 M_s} \quad (6)$$

Nanoferrites exhibit super paramagnetic behaviour, as indicated by the squareness ratio (<1). Magnetic spin surface effects are responsible for the "S"-shaped behaviour of the M-H loop. These effects affect the magnetic parameters of ferrites. Also, the squareness ratio value (<0.5) means that samples have a multi-domain structure. All examples have a multi-domain structure because their squareness ratios (<0.5) [38]. The M_r/M_s ratio can be used to estimate a material's toughness. A lower H_c value avoids magnetic and electrical losses, and a higher M_s value results in a higher spin current.

Table 3. Variation of saturation magnetization, Remanence magnetization, Coercivity, Squareness ratio, Bohr's magneton and anisotropy constant

Sr. No.	Comp. (x)	M_s (emu g^{-1})	M_r (emu g^{-1})	H_c	M_r/M_s	Bohors Magneton unit	Anisotropy Constant ($K = \frac{M_s H_c}{2}$ x 10^4)
1.	0.0	17.23	3.08	95.0	0.1787	671.58	827.47
2.	0.05	33.33	5.71	90.9	0.1713	1299.12	1459.52
3.	0.10	49.99	8.47	88.2	0.1694	1948.49	2071.08
4.	0.15	65.16	10.68	86.8	0.1639	2539.78	2666.99

Field Emission Scanning Electron Microscopy Analysis (FE-SEM)

Figure 5 shows the FE-SEM images of $Cu_{0.5}Mg_{0.5}Cr_{0.5}Ce_xFe_{1.5-x}O_4$ (x = 0.0, 0.05, 0.10, 0.15). From FE-SEM images, it was clear that the particles were spherical in nature. **Figure 7** also shows the histogram of FE-SEM and the obtained grain size of nano ferrites, which ranges from 90 nm to 60 nm. The average grain size decreases as Ce doping increases; this is due to an increase in the concentration of CeO_2. This shows the agglomeration of particles in the ferrite. The average grain size decreases with increasing doping concentration, as seen in XRD results.

Transmission Electron Microscopy (TEM)

Figure 8 shows the micrographs for $Cu_{0.5}Mg_{0.5}Cr_{0.5}Ce_xFe_{1.5-x}O_4$ (x = 0.0 and x = 0.15). Image J software was used to plot the histograms for these samples. The results revealed that the particles were spherical in shape with grain sizes between 55 nm and 48 nm. The results are good and in agreement with the XRD-calculated crystalline size. The histograms for these samples are shown in **Figure 8**.

Energy Dispersive X- ray spectroscopy (EDS)

The qualitative elemental analysis of samples from the $Cu_{0.5}Mg_{0.5}Cr_{0.5}Ce_xFe_{1.5-x}O_4$

series of nano ferrites is provided by energy dispersive X-ray spectroscopy. The EDS spectrum shown in **Figure 9** provides information about the existence and presence of all elements in the composition with no impurities. The weight percentage and atomic percentage of all elements are present in the ferrites shown in **Table 4** and **Table 5**, respectively.

Table 4. The elements of each sample composition $Cu_{0.5}Mg_{0.5}Cr_{0.5}Ce_xFe_{1.5-x}O_4$ nanoparticles analysed by (weight %) obtained by EDS

Sr. No	Concentration	Elements with weight %						Total Weight %
		O	Mg	Cr	Fe	Cu	Ce	
1	0.0	24.35	8.81	18.48	38.75	9.61	0	100
2	0.05	21.00	7.82	14.22	38.63	10.51	7.82	100
3	0.10	24.18	8.44	13.91	40.04	9.71	3.71	99.99
4	0.15	24.69	8.13	14.36	39.85	9.47	3.50	100

Table 5. The elements of each sample composition $Cu_{0.5}Mg_{0.5}Cr_{0.5}Ce_xFe_{1.5-x}O_4$ nanoparticles analysed by (Atomic %) obtained by EDS

Sr. No.	Concentration	Elements with atomic %						Total Weight %
		O	Mg	Cr	Fe	Cu	Ce	
1	0.0	49.34	11.74	11.52	22.49	4.90	0	99.99
2	0.05	46.53	11.41	9.69	24.52	5.87	1.98	100
3	0.10	50.01	11.49	8.85	23.72	5.06	0.88	100.01
4	0.15	50.74	10.99	9.08	23.47	4.90	0.82	100

Dielectric properties

Figure 10 (a and b) illustrates the dielectric constant and dielectric loss tangent as a function of frequency at room temperature. The dielectric constant decreases as frequency increases, then remains constant and becomes steady. Because of electronic, ionic, dipolar, and space charge polarization, the dielectric constant is greater at lower frequencies. However, as frequency increases, all polarization except space charge polarization decreases, and thus the dielectric constant decreases. The variation of dielectric permittivity with frequency indicates the dispersion due to the Maxwell–Wagner type of interfacial polarization in accordance with Koop's phenomenological theory. According to this theory, the conductivity of grain boundaries contributes more to the dielectric constant at lower frequencies. In this model, the dielectric structure is assumed to consist of well-conducting

grains that are separated by poorly conducting grain boundaries. The function of dielectric polarization in spinel ferrites is similar to that of electrical conduction. Dielectric permittivity variation can thus be linked to the collective behaviour of both types of electric charge carriers, electrons and holes. The dielectric constant is calculated using the following relationship:

$$\epsilon' = \frac{C \times d}{\epsilon_0 A} \quad (7)$$

Where, A is the pallet's cross-sectional area, C and d are the capacitance and thickness, respectively, and is the permittivity of free space.

The dielectric loss tangent also exhibits frequency dependence. It also shows that with an increase in frequency, the dielectric loss tangent also decreases, and at a certain frequency, it remains constant and steady. The dielectric loss tangent is calculated using the following relationship:

$$\tan\delta = \frac{\epsilon'}{\epsilon''} \quad (8)$$

Where tan δ is the dielectric loss tangent, $\boldsymbol{\epsilon}$' is the dielectric loss constant and $\boldsymbol{\epsilon}$" is the dielectric loss.

Conclusion

Cerium-ion doped Cu-Mg-Cr ferrite nanoparticles were synthesized using sol-gel synthesis, and XRD analysis confirmed the formation of a cubic spinel structure with the formation of the secondary phase of CeO_2. The lattice parameter increases (7.831 Å to 7.881 Å) with a decrease in crystalline size (28 nm to 26 nm). Both sides' hoping length increases. The spherical shape of the particles was confirmed by SEM and TEM measurements. The compositional analysis of the samples was confirmed by EDAX, and their observed and theoretical proportions are in good agreement with each other. VSM analysis revealed that, with cerium content, the saturation magnetization of the sample increased from17.23 emu g^{-1} to 65.16 emu gm^{-1}. Dielectric properties revealed the usefulness of high-frequency appliances is suggested by lower dielectric loss with increasing frequency.

Acknowledgement

We are grateful that Mr. Mahesh M. Gurav received financial support from the Mahatma Jyotiba Phule Research and Training Institute in Nagpur under the MJRF-2021 (MAHAHYOTI/Nag/Fellowship/2021-2022/1042 (589).

References

1. Bid, S. and Pradhan, S. K., *Mater. Chem. Phys.*, **2003**, 82 (1), 27-37.

https://doi.org/10.1016/S0254-0584(03)00169-X.

2. Vestal, C. R. and Zhang, Z. J., *J. Am. Chem. Soc.*, **2003**, 125 (32), 9828-9833. https://doi.org/10.1021/ja035474n.
3. Batoo, K. M., Kumar, S., Lee, C. G. and Alimuddin, *Curr. Appl. Phys.*, **2009**, 9 (4), 826-832. https://doi.org/10.1016/j.cap.2008.08.001.
4. Shirsath, S. E., Toksha, B. G., Kadam, R. H., Patange, S. M., Mane, D. R., Jangam, G. S. and Ghasemi, A., *J. Phys. Chem. Solids*, **2010**, 71 (12), 1669-1675. https://doi.org/10.1016/j.jpcs.2010.08.016.
5. Goodarz naseri, M., Saion, E., Ahangar, H., Shaari, A. and Hashim, M., *J. Nanomater.*, **2010**, 2010. https://doi.org/10.1155/2010/907686.
6. Dixit, G., Singh, J. P., Srivastava, R. C. and Agrawal, H. M., *J. Magn. Magn.*, **2013**, 345, 65-71. https://doi.org/10.1016/j.jmmm.2013.05.060.
7. Hankare , P. P., Patil, N. M., Patil, R. P., Patil, D. R. and Delekar, S. D., *J. Mater Sci Mater Electron.*, **2013**, 24 (10), 4028-4032. https://doi.org/10.1007/s10854-013-1357-1.
8. He , H. Y., *Part. Sci. Technol.*, **2015**, 34, 150713172707003. https://doi.org/10.1080/02726351.2015.1054970.
9. Rahimi, M., Kameli, P., Ranjbar, M., Hajihashemi, H. and Salamati, H., *J. Mater. Sci.*, **2013**, 48 (7), 2969-2976. https://doi.org/10.1007/s10853-012-7074-y.
10. Bhukal, S., Shivali, and Singhal, S., *Mater. Sci. Semicond. Process.*, **2014**, 26, 467-476. https://doi.org/10.1016/j.mssp.2014.05.023.
11. Dhiman, M., Sharma, R., Kumar, V. and Singhal, S., *Ceram. Int.*, **2016**, 42 (11), 12594-12605. https://doi.org/10.1016/j.ceramint.2016.04.115.
12. Shafa, M., Naz, M. Y., Ahmad, M. R., Khan, Y. and Ghaffar, A., HTMPS., **2018**, 37 (1), 89-95. https://doi.org/10.1515/htmp-2016-0037.
13. Elayakumar, K., Dinesh, A., Manikandan, A., Palanivelu, M., Kavitha, G., Prakash, S., Thilak Kumar, R., Jaganathan, S. K. and Baykal, A., *J. Magn. Magn.*, **2019**, 476, 157-165. https://doi.org/10.1016/j.jmmm.2018.09.089.
14. Dimri, M. C., Khanduri, H., Agarwal, P., Garg ,V., Mere, A. and Stern, R., *AIP Conf Proc.*, **2020**, 2265 (1), 030517. https://doi.org/10.1063/5.0016823.
15. Ghosh, M. P. and Mukherjee, S., *J. Mater Sci Mater.*, **2020**, 31 (8), 6207-6216. https://doi.org/10.1007/s10854-020-03174-4.
16. Pham, T. N., Huy, T. Q. and Le, A.-T., *RSC Advances*, **2020**, 10 (52), 31622-31661. https://doi.org/10.1039/d0ra05133k.

17. Pilania, G., Kocevski, V., Valdez, J. A., Kreller, C. R. and Uberuaga, B. P., *Commun. Mater.*, **2020**, 1 (1), 84. https://doi.org/10.1038/s43246-020-00082-2.
18. Elayakumar, K., Sathana, V. and Kumar, R. T., *J. Supercond. Nov. Magn.*, **2020**, 33 (7), 2171-2178. https://doi.org/10.1007/s10948-020-05475-5.
19. Qamar, S., Akhtar, M. N., Batoo, K. M. and Raslan, E. H., *Ceram. Int.*, **2020**, 46 (10, Part A), 14481-14487. https://doi.org/10.1016/j.ceramint.2020.02.246
20. Yu, L., Sun, A., Suo, N., Zuo, Z., Zhao, X., Zhang, W., Shao, L. and Zhang ,Y., *J. Mater Sci Mater Electron.*, **2020**, 31 (17), 14961-14976. https://doi.org/10.1007/s10854-020-04059-2.
21. McDonald, K. D. and Bartlett, B. M., *Inorg. Chem.*, **2021**, 60 (12), 8704-8709. https://doi.org/10.1021/acs.inorgchem.1c00663.
22. Srinivasamurthy, K. M., Angadi, V. J., Kubrin, S. P., Matteppanavar, S., Sarychev, D. A. and Rudraswamy, B., *J. Supercond. Nov. Magn.*, **2019**, 32 (3), 693-704. https://doi.org/10.1007/s10948-018-4752-2.
23. Zakir, R., S. Iqbal S., Rehman, A. U., Nosheen, S., Ahmad, T. S., Ehsan, N. and Inam, F., *Ceram. Int.*, **2021**, 47 (20), 28575-28583. https://doi.org/10.1016/j.ceramint.2021.07.016.
24. Soufi, A., Hajjaoui, H., Elmoubarki, R., Abdennouri, M., Qourzal, S. and Barka, N., *Appl. Surf. Sci. Tech.*, **2021**, 6:100145.https://doi.org/10.1016/j.apsadv.2021.100145.
25. Rabbani, A., Haghniaz, R., Khan, T., Khan, R., Khalid, A., Naz, S. S., Ul-Islam, M., Vajhadin, F. and Wahid, F., *RSC Advances*, **2021**, 11 (3), 1773-1782. https://doi.org/10.1039/d0ra08417d.
26. Shah, M. S., Aman, S., Ahmad, N., Tahir, M. B., Alrowaili, Z. A., Al-Buriah,i M. S., H. Farid M. T., Khosa, R. Y., Hussein, E. E., Elnaggar, A. Y. and El-Bahy, Z. M., *J. Taibah Univ. Sci.*, **2021**, 15 (1), 798-804. https://doi.org/10.1080/16583655.2021.2005321.
27. Jahan, N., Khan, M. N. I. and Khandaker, J. I., *ACS Omega*, **2021**, 6 (48):32852-32862. https://doi.org/10.1021/acsomega.1c04832.
28. Mushtaq K, S.S., Saeed, T., Ul-Hamid, A., Abbasi, B. H., Ahmad, N., Khalid, W., Atif, M., Ali, Z., Abbasi, R. Beilstein J. Nanotechnol., **2021** (12). https://doi.org/doi:doi:10.3762/bjnano.12.99.
29. Savita, A. M., Singh, R. K., Kumar, S. S., Satyapal, H. and Kumar, G., *Abstracts of International Conferences & amp; Meetings*, **2021**, 1 (5), 27.
30. Kousar, T., Aadil, M., Zulfiqar, S., Warsi, M. F., Ejaz, S. R., Elnaggar, A. Y., Fallatah,

A. M., El-Bahy, S. M. and Mahmood, F., *Ceram. Int.*, **2022**, 48 (8), 11858-11868. https://doi.org/10.1016/j.ceramint.2022.01.057.

31. Almessiere, M. A., Güner, S., Slimani, Y., Baykal, A., Shirsath, S. E., Korkmaz, A. D., Badar R. and Manikandan, A., *J. Mol. Struct.*, **2022**, 1248, 131412. https://doi.org/10.1016/j.molstruc.2021.131412.
32. Dinesh, A., Kanmani Raja, K., Manikandan, A., Almessiere, M. A., Slimani, Y., A., Baykal, H. Alorfi, Saeed., Hussein, M. A. and Khan, A., *J. Mater. Res. and Technol.*, **2022**, 18, 5280-5289. https://doi.org/10.1016/j.jmrt.2022.04.121.
33. Kumar, N., Archana, Singh R. K., Kumar, V. and Das, S. B., *J. Mater Sci Mater Electron.*, **2022**, 33 (9), 6131-6149. doi:10.1007/s10854-022-07790-0.
34. Nikmanesh, H., Jaberolansar, E., Kameli, P., Ghotbi Varzaneh, A., Mehrabi, M., Shamsodini, M., Rostami, M., Orue, I. and Chernenko, V., *J. Magn.Magn. Mater.*, **2022**, 543, 168664. https://doi.org/10.1016/j.jmmm.2021.168664.
35. Slimani, Y., Almessiere, M. A., Guner, S., Aktas, B., Shirsath, S. E., Silibin, M. V., Trukhanov, A. V. and Baykal, A., *ACS Omega*, **2022**, 7 (7):6292-6301. https://doi.org/10.1021/acsomega.1c06898.
36. Wang, J., Sun A., Jiang, Y., Huang, X., Shao, L. and Zhang, Y., *J. Mater Sci Mater electron*, **2022**, https://doi.org/10.1007/s10854-022-08150-8.
37. Ahmad, D., Mehboob, N., Zaman, A., Ahmed, N., Ahmed, K., Mushtaq, M., Althubeiti, K., Ali, A., Sultana, F. and Bashir, K., *coatings*, **2021**, 11 (10). https://doi.org/10.3390/coatings11101156.
38. Balsure, S., More, V., Kadam, S., Kadam, R., Kadam, A., *Eng.sci.*, **2023,** 21, 774. http://dx.doi.org/10.30919/es8d774.

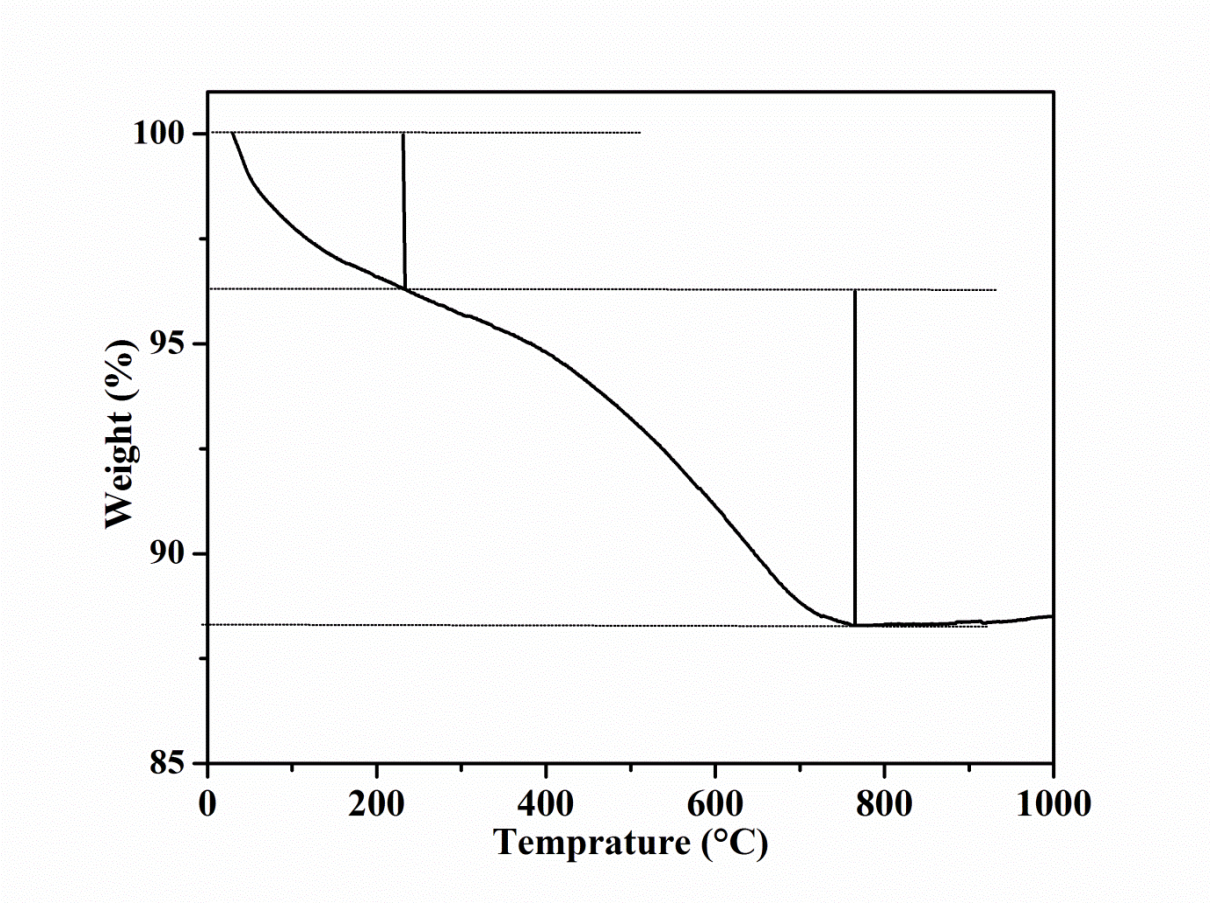

Figure 1. TGA Spectrum of $Cu_{0.5}Mg_{0.5}Cr_{0.5}Fe_{1.5}O_4$ nanoparticle

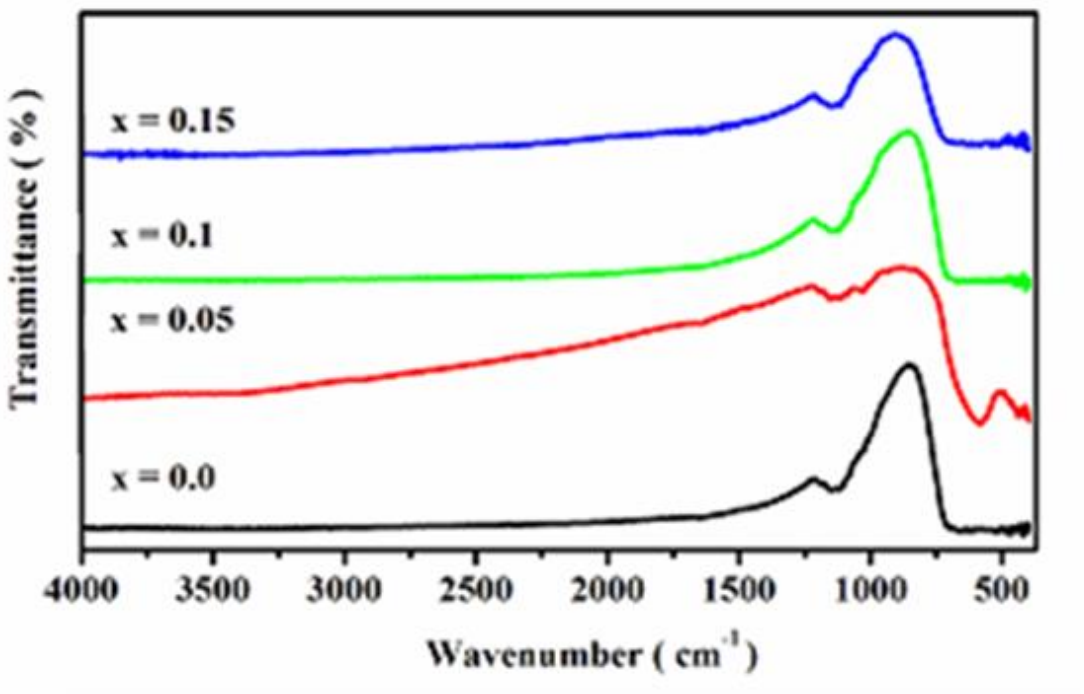

Figure 2. FT- IR spectra of $Cu_{0.5}Mg_{0.5}Cr_{0.5}Ce_xFe_{1.5-x}O_4$ nanoparticles

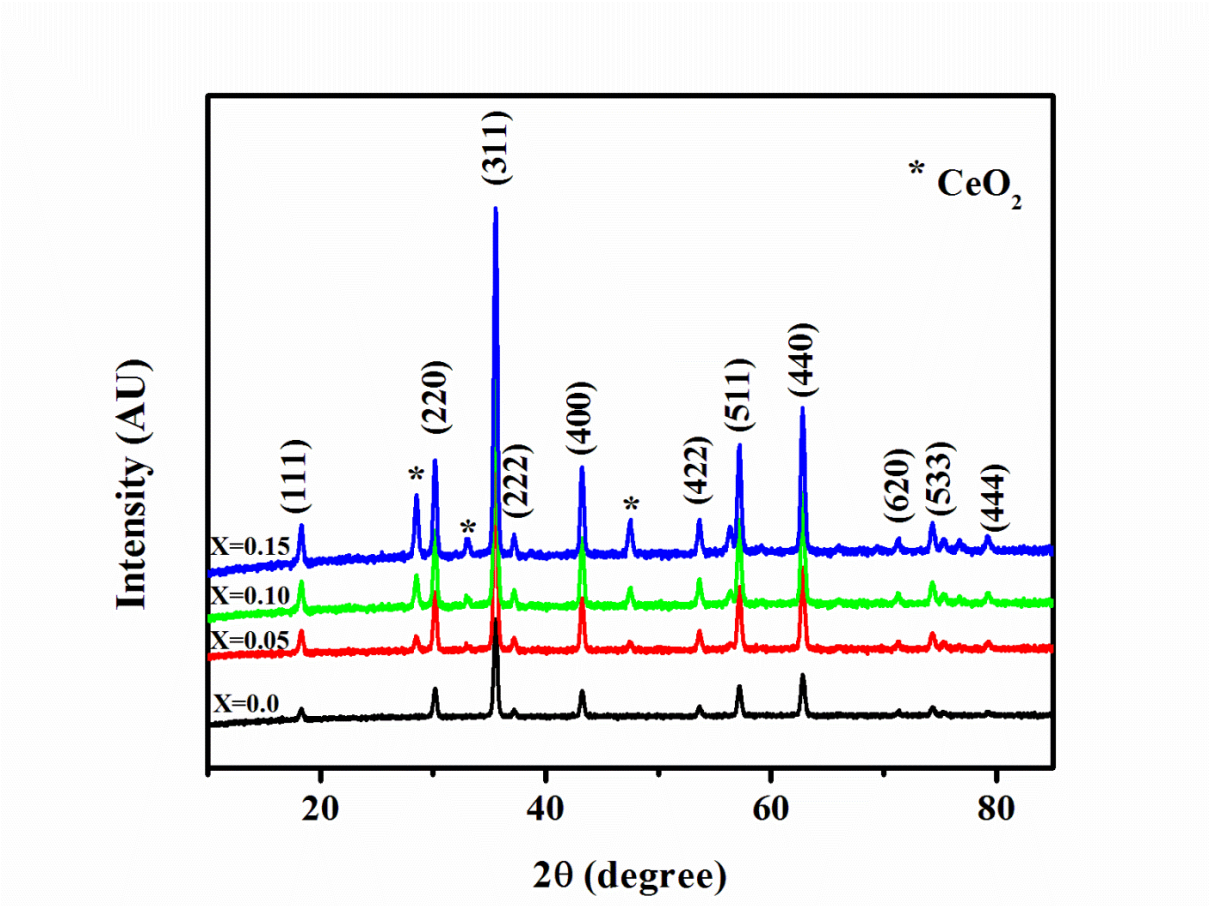

Figure 3. X-Ray diffraction pattern for $Cu_{0.5}Mg_{0.5}Cr_{0.5}Ce_xFe_{1.5-x}O_4$ nanoparticles

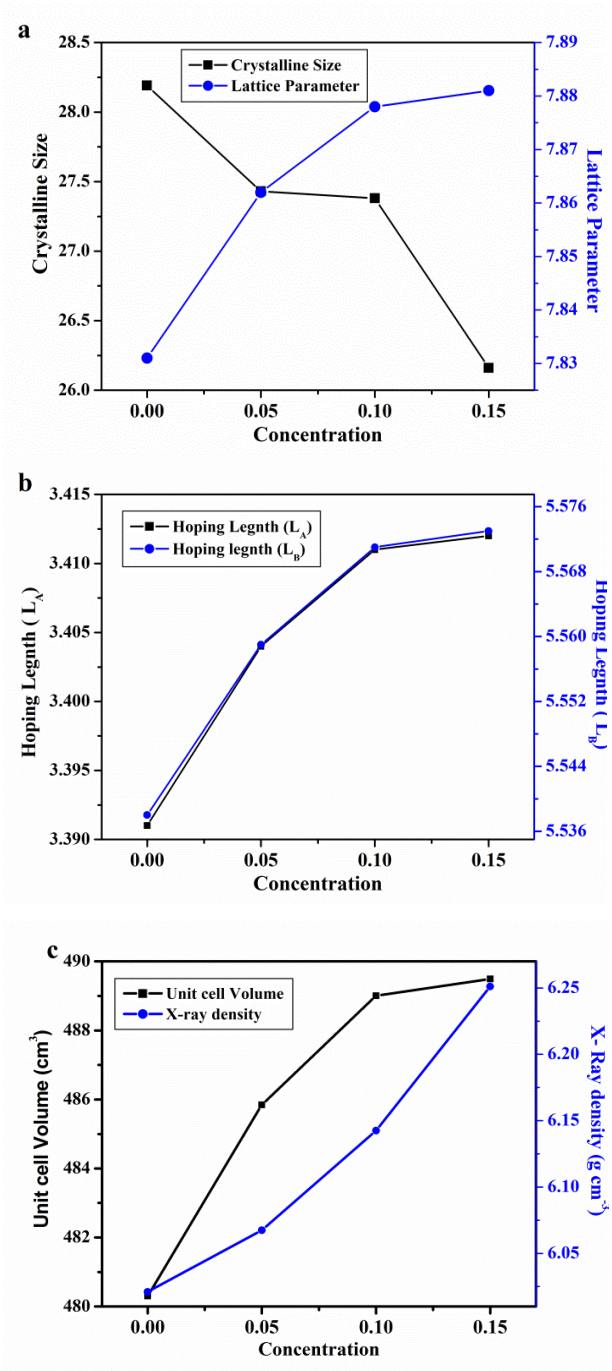

Figure 4. a) Crystalline size and lattice parameter b) Hoping length c) unit cell volume and X- ray density Vs Concentration of $Cu_{0.5}Mg_{0.5}Cr_{0.5}Ce_xFe_{1.5-x}O_4$ nanoparticles

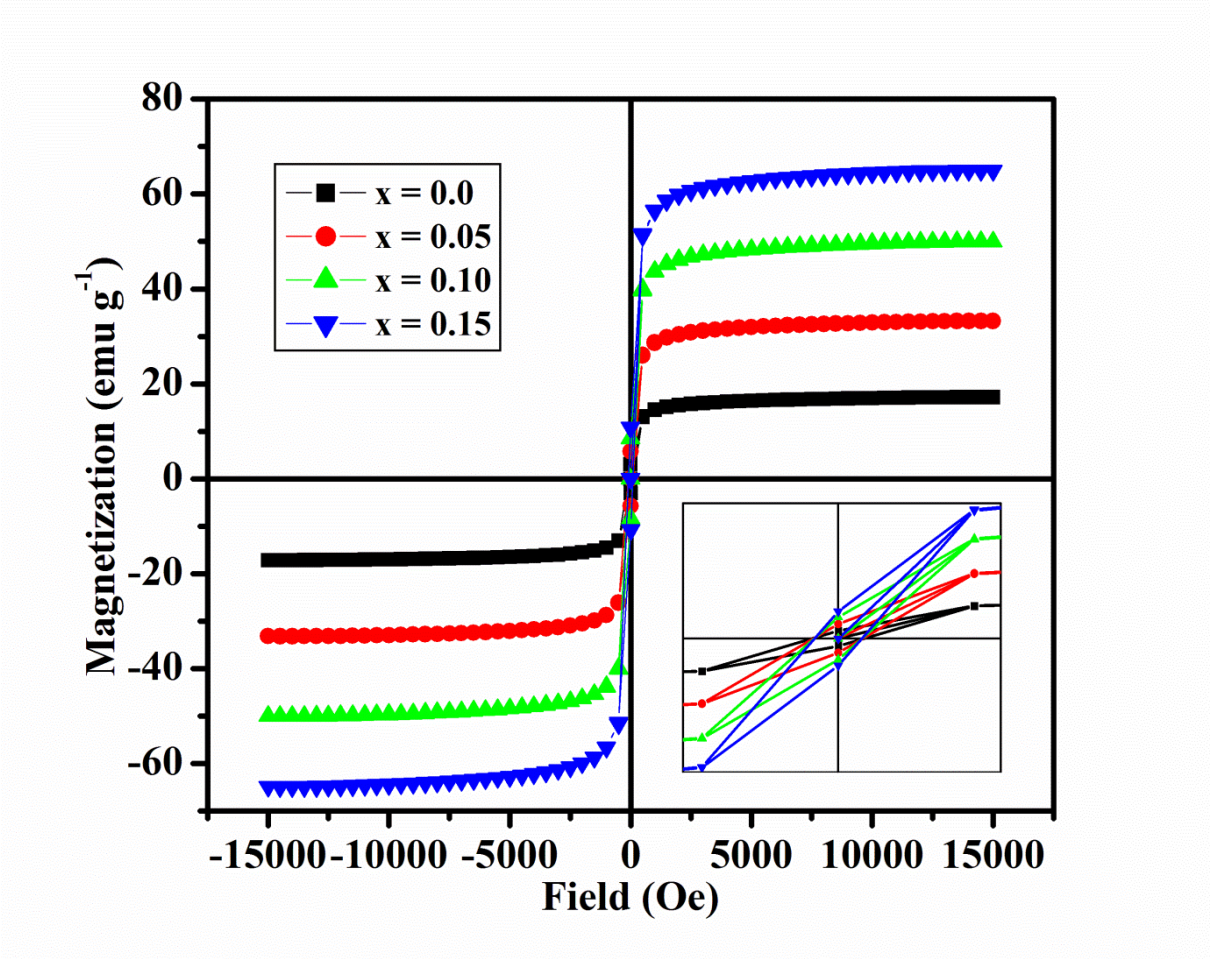

Figure 5. VSM plot of the $Cu_{0.5}Mg_{0.5}Cr_{0.5}Ce_xFe_{1.5-x}O_4$ nanoparticles

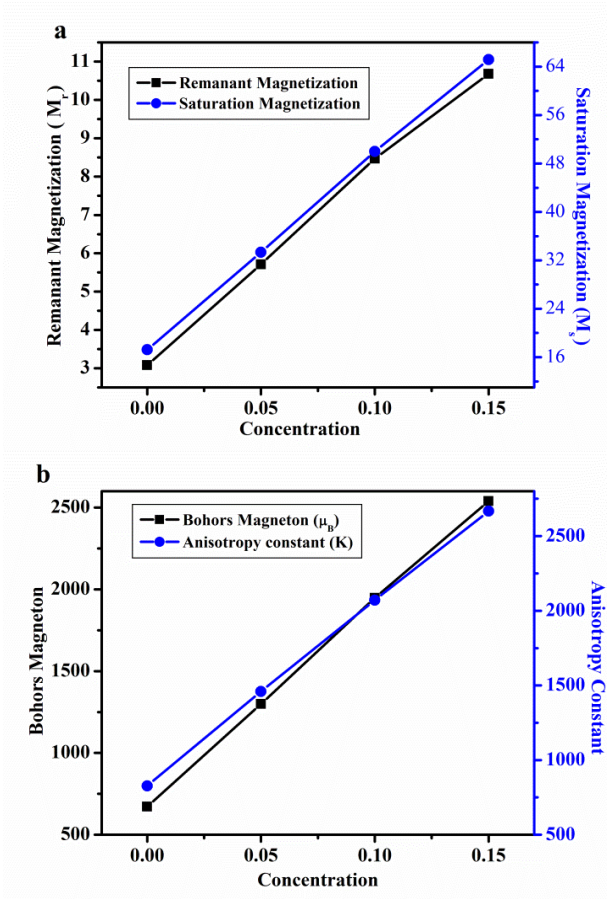

Figure 6. a) Remnant Magnetization and Saturation Magnetization

b) Bohrs Magneton, Anisotropy constant against concentration

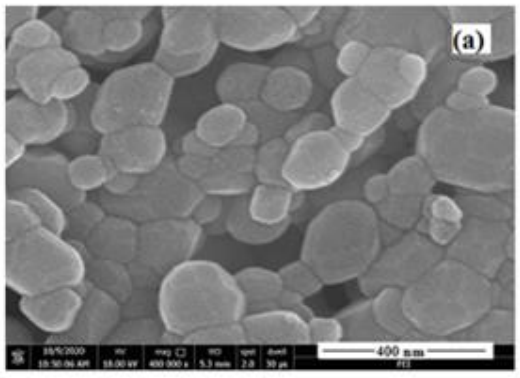

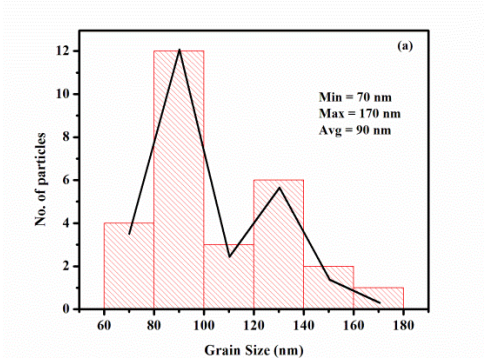

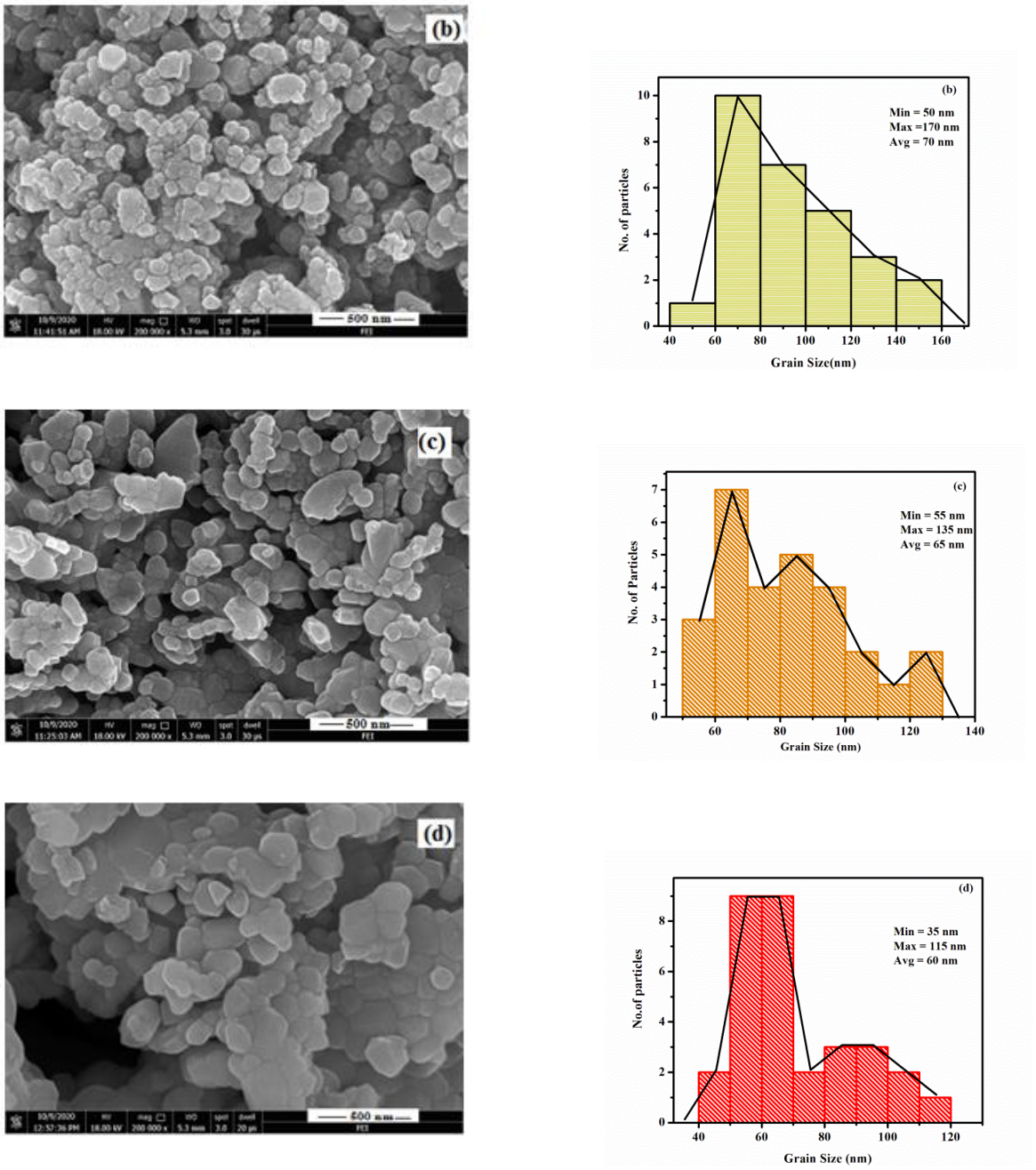

Figure 7. SEM images and histograms of $Cu_{0.5}Mg_{0.5}Cr_{0.5}Ce_xFe_{1.5-x}O_4$ nanoparticles

a) x = 0.0 b) x = 0.05 c) x = 0.10 d) x = 0.15

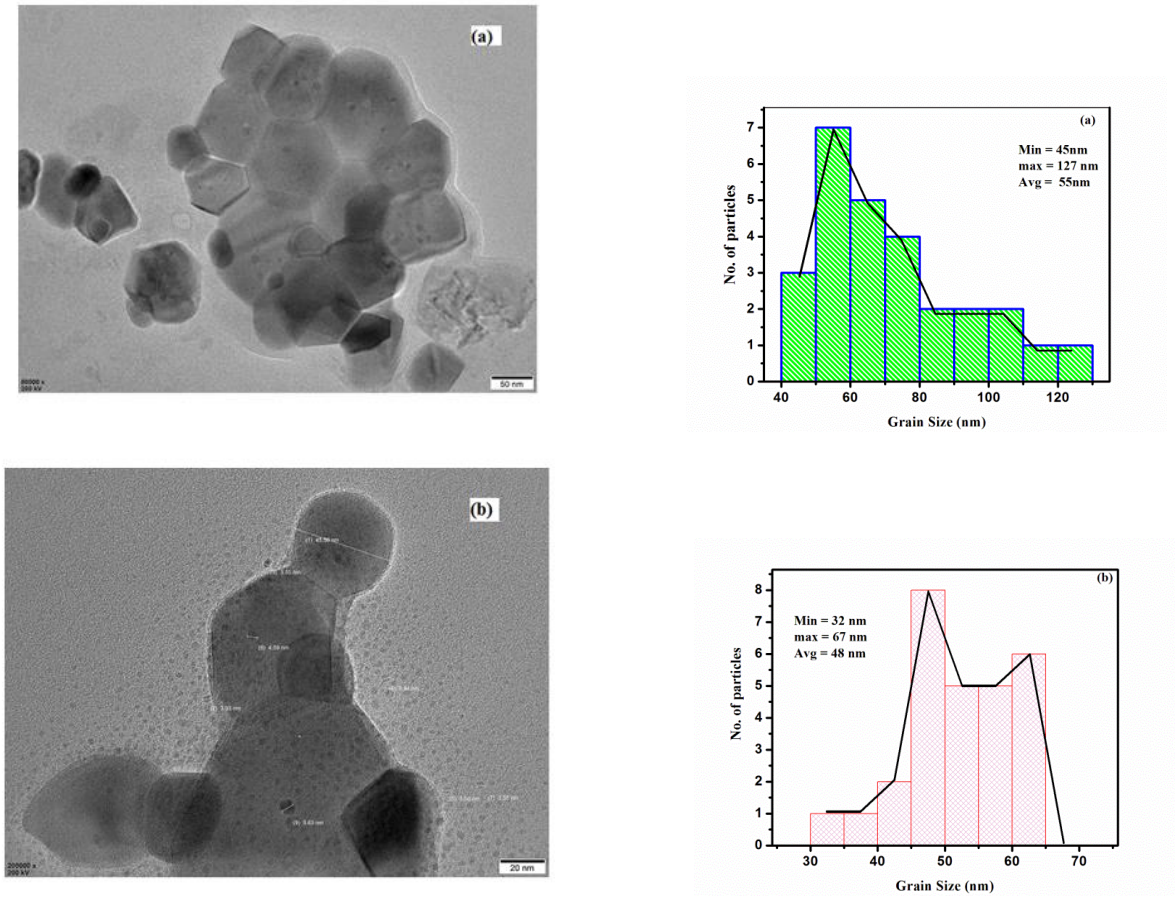

Figure 8. HR-TEM images and histograms of $Cu_{0.5}Mg_{0.5}Cr_{0.5}Ce_xFe_{1.5-x}O_4$ nanoparticles

a) x = 0.0 b) x = 0.15

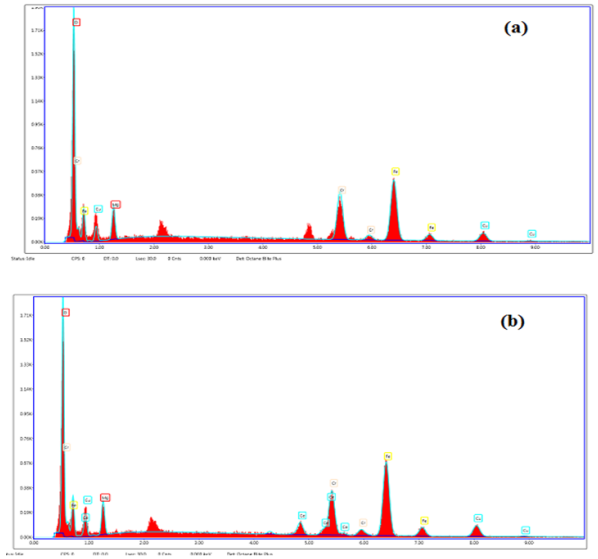

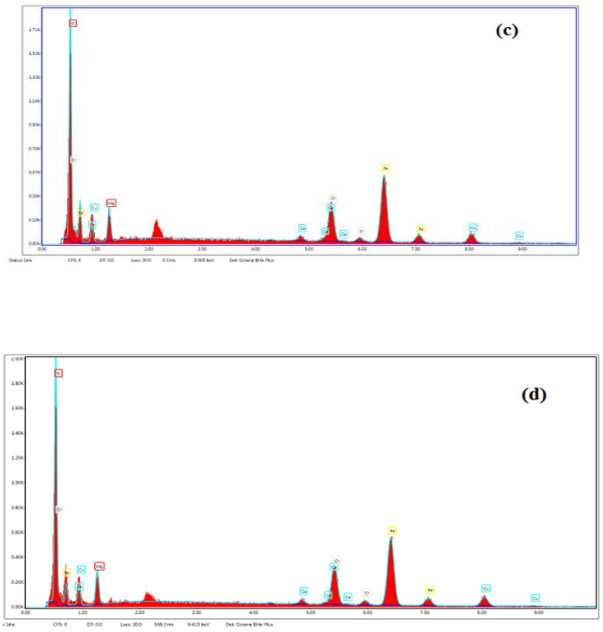

Figure 9. EDS pattern of $Cu_{0.5}Mg_{0.5}Cr_{0.5}Ce_xFe_{1.5-x}O_4$
a) x = 0.0 b) x = 0.05 c) x = 0.1 d) x= 0.15

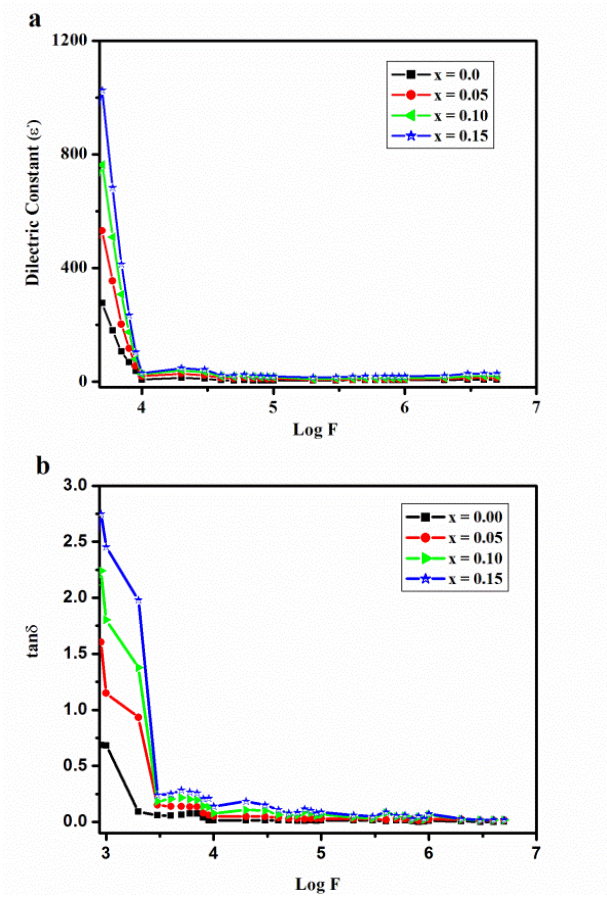

Figure 10. a) Dielectric constant, b) Dielectric loss tangents against frequency data of $Cu_{0.5}Mg_{0.5}Cr_{0.5}Ce_xFe_{1.5-x}O_4$